UNIVERSITY OF CALIFORNIA SAN DIEGO

An MRI-CFD Prospective Analysis of Longitudinal Changes in Chiari Malformation

A dissertation submitted in partial satisfaction of the
requirements for the degree Master of Science

in

Engineering Sciences (Aerospace Engineering)

by

Madison Sznicer

Committee in charge:

Professor Antonio L. Sanchez, Chair
Professor Eugene R. Pawlak
Professor Oliver T. Schmidt

2026

The Dissertation of Madison Sznicer is approved, and it is acceptable in quality and form for publication on microfilm and electronically.

University of California San Diego

2026

TABLE OF CONTENTS

LIST OF FIGURES

LIST OF TABLES

ACKNOWLEDGEMENTS

I would like to acknowledge Professor Antonio L. Sanchez for his support as the chair of my committee. I have greatly appreciated the opportunity to work with and learn from him. I would also like to express my sincere gratitude to Dr. Guillermo L. Nozaleda for his mentorship throughout this research. His guidance at every stage was essential to the completion of this work, and I am especially grateful for everything I have learned from him. I extend my appreciation to collaborators Francisco J. Parras-Martos, Dr. Cándido Gutiérrez-Montes, and Dr. Wilfried Coenen, whose contributions have brought valuable and interesting perspectives to the discussions surrounding this work. Finally, I would like to thank my friends, particularly Katherine Sikorski, as well as my parents and sister for their constant support and encouragement throughout my graduate studies.

ABSTRACT OF THE DISSERTATION

An MRI-CFD Prospective Analysis of Longitudinal Changes in Chiari Malformation

by

Madison Sznicer

Master of Science in Engineering Sciences (Aerospace Engineering)

University of California San Diego, 2026

Professor Antonio L. Sanchez, Chair

Abstract

Chiari malformation type I (CM-I) is characterized by herniation of the cerebellar tonsils past the foramen magnum into the upper spinal canal. This descent can obstruct cerebrospinal fluid (CSF) flow. A large fraction of CM-I patients develop syringomyelia, in which a fluid-filled cavity, or syrinx, forms within the spinal cord. The mechanisms governing syrinx formation remain incompletely understood, although abnormal CSF dynamics associated with CM-I may play an important role. One leading hypothesis proposes that the pulsating cerebellar tonsils create amplified pressure waves in the spinal subarachnoid space that promote fluid transport into the spinal cord. However, some aspects of altered CSF dynamics in CM-I and the mechanisms underlying syrinx formation remain unexplained. This work characterizes cerebellar tonsillar motion, cervical CSF flow, and craniocervical pressure dynamics

before and after posterior fossa decompression in pediatric CM-I patients. Cardiac-gated phase-contrast magnetic resonance imaging (PC-MRI) was used to quantify tonsillar motion and cervical CSF flow. These measurements, together with T2-weighted MRI, were used to construct patient-specific computational fluid dynamics (CFD) models to evaluate pressure fields and longitudinal impedance, a pressure-based measure of resistance to oscillatory flow. Our results reveal that surgical decompression alters the relationship between tonsillar motion and cervical CSF flow. Most notably, postoperative cervical CSF flow exhibits more balanced bidirectional oscillations and becomes less synchronized with tonsillar motion than in the preoperative state, suggesting that postoperative CSF flow is less influenced by piston-like tonsillar displacement. In addition, the maximum longitudinal pressure difference exhibits variable changes across subjects, while longitudinal impedance consistently decreases following decompression, indicating reduced resistance to oscillatory CSF flow. These findings provide insight into the physiological effects of posterior fossa decompression and provide an MRI-informed CFD framework for future investigations of CM-I pressure dynamics and the mechanism underlying syrinx formation.

1 Background

Chiari Malformation Type I (CM-I) is a neurological condition characterized by herniation of the cerebellar tonsils (the lower part of the cerebellum) past the base of the skull into the upper spinal canal. This descent can obstruct the subarachnoid space (SAS) at the craniocervical junction [1, 2] and alter the normal cerebrospinal fluid (CSF) flow driven by cardiac and respiratory cycles [3]. Symptoms commonly linked to CM-I are headaches, neck pain, dizziness, and balance issues. A substantial subset of patients develop syringomyelia, in which a fluid-filled cavity (syrinx) forms within the spinal cord [4]. Syringomyelia may lead to chronic pain, sensory loss, muscle weakness, scoliosis, and progressive myelopathy.

The mechanisms governing syrinx formation remain incompletely understood, although many studies suggest that abnormal CSF dynamics play an important role in fluid accumulation. Experimental studies have shown that syrinx fluid enters the spinal cord through perivascular spaces [5–7], fluid-filled channels surrounding penetrating blood vessels that provide pathways for CSF exchange between the SAS and spinal cord. Under healthy conditions, transmedullary fluid inflow and outflow through these spaces remain balanced, whereas altered CSF dynamics in CM-I may disrupt this bidirectional exchange and contribute to syrinx formation [8–10].

Several theories have been proposed to explain how tonsillar herniation and obstruction at the craniocervical junction may lead to abnormal CSF flow in CM-I patients. A widely cited hypothesis is that of Oldfield et al., which proposes that the pulsating cerebellar tonsils act as a piston, generating elevated pressure waves in the spinal subarachnoid CSF that promote fluid entry through the perivascular pathways [11]. Although clinical observation supports the presence of these tonsillar pulsations, many questions remain unanswered. A key unresolved issue is how there can be a net flow of CSF from the SAS into the syrinx, despite studies consistently reporting the mean pressure in the syrinx to be higher than that of the surrounding SAS [12]. In addition, distinctions in CSF dynamics between CM-I patients who

develop syringomyelia and those who do not remain unclear [4]. Overall, no single theory fully explains all presentations of syringomyelia, and further investigation is needed to determine which hydrodynamic factors are most relevant to syrinx progression and surgical decision-making. Phase-contrast magnetic resonance imaging (MRI) has been widely used to characterize CM-I flow abnormalities [13], as it allows for noninvasive cardiac-gated measurements of CSF velocity. PC-MRI studies have reported abnormal peak velocities in CM-I patients relative to healthy subjects, many demonstrating elevated peak velocities [2, 14] while others present reduced peaks [15]. CM-I patients also exhibit increased spatial variability in CSF flow, such as high-velocity anterior jets and reduced posterior flow, unlike the more uniform velocity distributions seen in healthy subjects [16]. These flow irregularities are often partially restored toward normal after posterior fossa decompression, which is the standard treatment for CM-I. Temporal differences have also been observed, with CM-I patients presenting earlier onsets and earlier peaks of caudal CSF flow compared to healthy subjects [10], although few studies have examined how these timing characteristics change after surgical intervention.

More recent CM-I studies combine PC-MRI measurements with computational fluid dynamics (CFD) for a more comprehensive analysis of CSF flow. In particular, 2D PC-MRI often provides velocity measurements only at discrete locations and in the direction perpendicular to the imaging plane, while CFD can reconstruct full spatially and temporally resolved velocity fields. CFD also allows for noninvasive computations of pressure gradients, which would otherwise require lumbar puncture for direct measurement [17]. These qualities have proved useful for CM-I studies, allowing for new pressure-based hydrodynamic markers such as longitudinal impedance [18–20], which has been associated with symptom severity.

In this study, PC-MRI measurements from seven pediatric CM-I patients are analyzed to characterize tonsillar motion and CSF flow before and after decompression surgery. The pediatric population is of particular interest, as studies have found pediatric CM-I subjects to more frequently present with syringomyelia and scoliosis [21, 22]. These measurements are then combined with T2-weighted MRI to reconstruct patient-specific geometries and develop CFD simulations of CSF flow in the craniocervical SAS. By characterizing preoperative and postoperative CSF dynamics, this work aims to improve understanding of the physiological changes associated with decompression surgery and provide a foundation for future CFD investigations of CM-I and syringomyelia.

2 Methods

2.1 Patient cohort

Seven pediatric patients diagnosed with CM-I participated in this study. The sex annd age of each subject, as well as the symptoms they experience, are listed in Table 1. Subject 6 of this study had a clear syrinx presentation. All experimental protocols were approved by University of Utah and Intermountain Institutional Review Boards (IRB_00178613), and all procedures were conducted in accordance with relevant guidelines and regulations. Written informed consent was obtained from the parents or legal guardians of all participants prior to enrollment in the study.

Table 1. Demographic and clinical characteristics of the study cohort.

			Symptoms					
Subject	Sex	Age (years)	Posterior neck pain	Sensory symptoms or deficits	Cranial neuropathy	Swallowing difficulty	Valsalva-induced headache	Non-Valsalva-induced headache
1	F	15	Y	Y	N	N	Y	N
2	F	17	Y	N	Y	N	Y	N
3	F	17	N	Y	N	N	Y	N
4	M	16	N	N	N	N	Y	N
5	F	12	N	Y	N	Y	Y	N
6	F	14	N	Y	N	N	N	Y
7	F	14	N	Y	N	Y	Y	Y

2.2 Magnetic resonance imaging

Magnetic resonance imaging was performed on a 3T GE Architect scanner with software version MR30.1. Anatomical images of the craniocervical region were obtained using a three-dimensional sagittal T2-weighted Cube sequence with fat suppression. Imaging was performed with a 19-channel head-and-neck coil, along with a 40-channel GEM posterior array for the rest of the spine. For all patients, the

T2-weighted images were acquired using flip angle = 90°, matrix size 512 × 512, and slice thickness 0.8 mm. The patient-specific reptition time (TR), echo time (TE), and in-plane resolution are listed in Table 2. Note that the preoperative anatomical T2-weighted images for subject 1 were unavailable for analysis due to poor image quality, so these parameters are not reported. In addition, postoperative MRI measurements for subjects 5 and 7 had not yet been acquired at the time of this study.

Table 2. Patient-specific TR, TE, and in-plane resolution for the three-dimensional sagittal T2-weighted Cube sequence.

a) Preoperative

Subject	TR [ms]	TE [ms]	In-plane resolution [mm^2]
1	N/A	N/A	N/A
2	2834	120.6	0.508×0.508
3	1502	122.8	0.469×0.469
4*	4.71	2.1	0.352×0.352
5	1500	118.1	0.469×0.469
6	1500	123.1	0.429×0.429
7	1500	118.3	0.469×0.469

*Preoperative anatomical images for subject 4 were acquired using a FIESTA sequence rather than T2-weighted.

b) Postoperative

Subject	TR [ms]	TE [ms]	In-plane resolution [mm^2]
1	1000	82.8	0.977× 0.977
2	1500	122.2	0.508×0.508
3	1500	116.7	0.469×0.469
4	1864	123.0	0.430×0.430
6	2229	121.8	0.430×0.430

At three axial locations of the cervical canal, two-dimensional cardiac-gated PC-MRI acquisitions were performed. One acquisition was positioned at the foramen magnum (FM) to quantify tonsillar motion. The other two acquisitions were positioned at one intermediate cervical level (C1-C2 or C2-C3) and at the C3-C4 level to quantify CSF flow. A representative image of the PC-MRI acquisition locations used are shown in Figure 1.

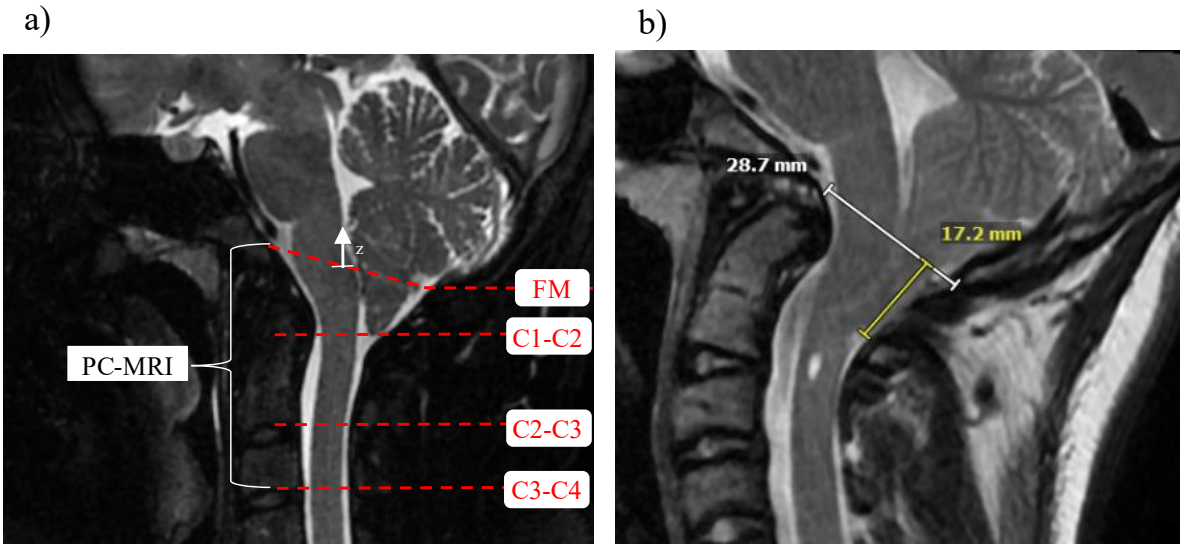

Figure 1. Sagittal T2-weighted MRI illustrating (a) the locations of the four PC-MRI acquisition planes at the FM, C1–C2, C2–C3, and C3–C4, and (b) the degree of tonsillar descent measured from the McRae line.

The PC-MRI sequence used through-plane velocity encoding to acquire the velocity component normal to each measurement plane. For all patients, the PC-MRI parameters were TR = 27.0 ms, flip angle = 10°, matrix size 512 × 512, in-plane resolution 0.391 ×0.391 mm^2, and slice thickness 4 mm. The patient-specific TE for each imaging plane is listed in Table 3, along with the heart rate of the subjects during each measurement. For all patients, the FM encoding velocity was set to VENC = 5, with the exception of the preoperative scans of subject 1 (VENC = 15) and subject 2 (VENC = 10). The encoding velocity at all lower cervical levels was VENC = 10. The physiological condition during image acquisition was free-breathing with no sedation. Retrospective cardiac gating was achieved through peripheral pulse gating, with 30 cardiac phases reconstructed per cycle. Note that cardiac-gated PC-MRI measurements were not acquired preoperatively for subject 4.

Table 3. Patient-specific PC-MRI acquisition parameters for each imaging plane.

a) Preoperative

Subject	Imaging plane	TE (ms)	Heart rate (bpm)
1	FM	7.84	66
	C1–C2	8.12	58
	C3–C4	8.14	58
2	FM	8.50	67
	C1–C2	8.15	69
	C3–C4	8.23	68
3	FM	9.35	105
	C2–C3	8.21	92
	C3–C4	8.21	98
4	N/A	N/A	N/A
	N/A	N/A	N/A
	N/A	N/A	N/A
5	FM	9.22	88
	C2–C3	8.22	82
	C3–C4	8.22	72
6	FM	9.25	93
	C2–C3	8.22	98
	C3–C4	8.22	93
7	FM	9.19	62
	C2–C3	8.12	60
	C3–C4	8.12	64

b) Postoperative

Subject	Imaging plane	TE (ms)	Heart rate (bpm)
1	FM	9.45	75
	C1–C2	8.13	78
	C3–C4	8.14	80
2	FM	9.39	120
	C2–C3	8.17	157
	C3–C4	8.18	107
3	FM	9.32	175
	C2–C3	8.14	92
	C3–C4	8.14	98
4	FM	9.78	52
	C2–C3	8.18	51
	C3–C4	8.19	50
6	FM	9.25	89
	C2–C3	8.32	92
	C3–C4	8.28	88

2.3 Image processing

2.3.1 PC-MRI: Extraction of flow metrics

Cerebellar tonsillar motion and cervical CSF flow were quantified by extracting metrics from PC-MRI measurements using an in-house MATLAB code developed in a previous study [16], where the methodology is described in detail. In short, the cerebellar tonsils and CSF space were manually contoured in each measurement plane to define region of interest (ROI) masks, and the normal velocity component was obtained for each pixel within the ROIs. Spatial filtering, outlier removal, and phase-unwrapping methods were applied to reduce spurious measurements and correct velocity aliasing.

For each imaging plane, $u_{j,n}$ represents the filtered and de-aliased velocity at pixel $j \in [1,2,...,N_p]$ and cardiac phase $n \in [1,2,...,30]$, where N_p is the total number of pixels in the ROI mask, and the 30 cardiac phases span one cardiac cycle of period T. The time-resolved velocity at each pixel was reconstructed using a Fourier approximation with $M = 5$ modes, such that

$$u_j(t) = \sum_{k=-M}^{M} c_{j,k} \exp\left(\frac{2\pi i k t}{T}\right), \tag{2.1}$$

where $c_{j,k}$ are the complex Fourier coefficients for pixel j and mode k.

At the FM level, a representative velocity of the tonsils was determined by spatially averaging the reconstructed velocity over the tonsillar ROI according to

$$\bar{u}_{\mathrm{t}}(t) = \frac{\sum_{j=1}^{N_{p,t}} u_j(t) A_j}{\sum_{j=1}^{N_{p,t}} A_j}, \tag{2.2}$$

where $N_{p,t}$ is the number of pixels in the tonsillar ROI and A_j is the area of pixel j. This area-averaged velocity characterizes the bulk motion of the tonsils throughout the cardiac cycle. The total tonsillar displacement over one cardiac cycle was computed by integrating the magnitude of the spatially-averaged tonsillar velocity,

$$\Delta z = \int_0^T |\bar{u}_{\mathrm{t}}(t)|\, dt. \tag{2.3}$$

At the lower cervical levels, CSF volumetric flow rate waveforms were obtained by integrating the velocity $u_j(t)$ over the segmented CSF region,

$$Q_{CSF}(t) = \sum_{j=1}^{N_{p,c}} u_j(t) A_j, \tag{2.4}$$

where $N_{p,c}$ is the number of pixels in the CSF region. The CSF stroke volume, or the net volume of CSF moved during one cardiac cycle, is computed as

$$V_s = \frac{1}{2} \int_t^{t+T} |Q_{CSF}(t)| \, dt. \tag{2.5}$$

Finally, to quantify the spatial variability of the CSF velcoity field, the ratio of peak to mean velocity magnitude, $u_{peak}/|\bar{u}|$, was evaluated at the time of peak systolic flow. u_{peak} is the maximum velocity u_j within the CSF ROI, and the spatially averaged mean velocity magnitude was computed as

$$|\bar{u}| = \frac{\sum_{j=1}^{N_{p,c}} |u_j| A_j}{\sum_{j=1}^{N_{p,c}} A_j}. \tag{2.6}$$

2.3.2 T2-weighted MRI: CSF space segmentation

T2-weighted images were used to segment the craniocervical CSF space, from the mid-cervical spine to 5-10 mm above the FM. Initial segmentation below the FM was performed automatically using Spinal Cord Toolbox (SCT) [23], and the region above was manually segmented in 3D Slicer [24]. The final segmentation was exported as a surface mesh for subsequent volume meshing. The T2-weighted sagittal images were also used to extract the tonsillar descent z by measuring the distance from the FM (the McRae line) to the inferior tip of the tonsils, as shown in Figure 1.

2.4 Computational modeling

The segmentation of the CSF space was truncated at the FM and C3–C4 levels to obtain the computational domain, defined in ANSYS SpaceClaim (2024 R1) and shown in Figure 2. Microanatomical features, such as nerve roots, denticulate ligaments, and arachnoid trabeculae, were not included in the models. While recent work has demonstrated the importance of denticulate ligaments in particular [16], their inclusion was beyond the scope of the present study. Meshing was subsequently performed in ANSYS Fluent Meshing (2024 R1) using unstructured polyhedral elements, following the mesh parameters detailed

in a previous study [16].

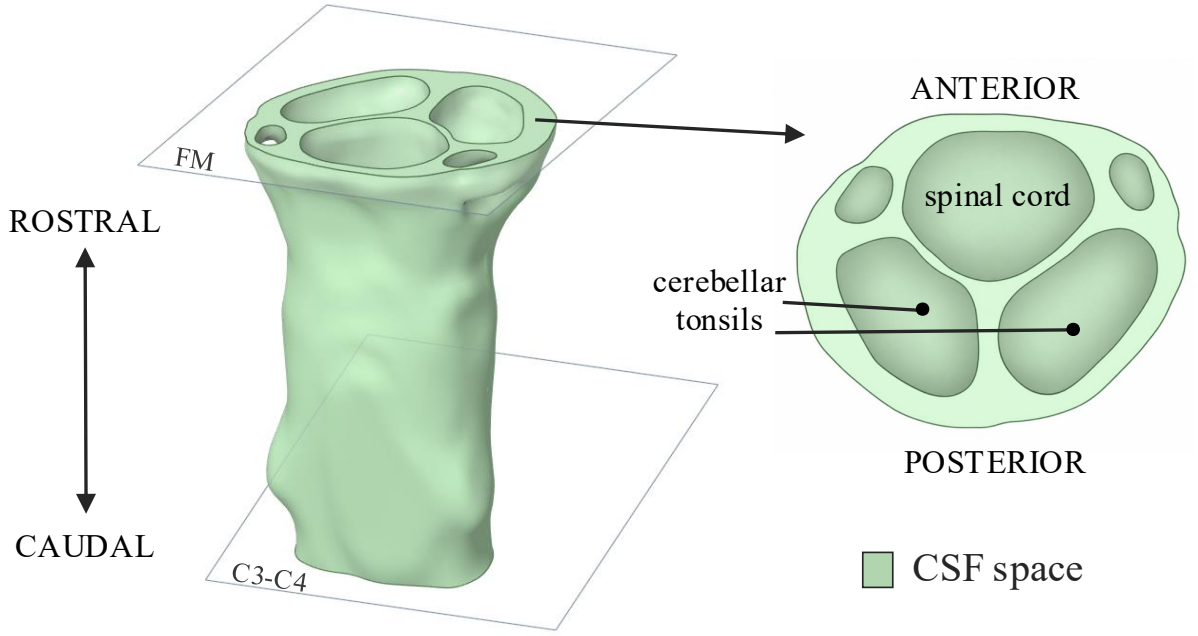

Figure 2. T2-weighted MRI-informed computational domain of the craniocervical CSF space extending from the FM to C3–C4 level.

The finite-volume solver ANSYS Fluent (2024 R1) was used to perform flow simulations, modeling CSF as a Newtonian fluid with density $\rho \simeq 1000$ kg/m^3 and kinematic viscosity $\nu \simeq 0.7 \times 10^{-}6$ m $^2/$s. The flow was modeled as laminar, and the incompressible Navier-Stokes equations were solved with a time-implicit, second order accurate scheme in space and time, using the COUPLED algorithm for velocity-pressure coupling. Each cardiac cycle with period T was discretized into 100 time steps, with 10 iterations per step. The simulations used steady-state initialization and were run over two cardiac cycles, with the second cycle used for subsequent analysis. The boundary conditions prescribed were a zero-pressure condition at the outlet (FM), as well as a spatially resolved velocity distribution at the inlet (C3-C4) obtained from the PC-MRI measurements.

A notable pressure-based metric obtained from the CFD simulations is the longitudinal impedance, a frequency-domain quantity that characterizes resistance to oscillatory CSF flow and reflects the influence of the craniocervical geometry. Following the methodology of Martin et al. [18], longitudinal impedance is computed by combining the CSF pressure field obtained from CFD with the PC-MRI-informed volumetric

flow rate. First, the impedance modulus Z_L is computed as

$$Z_{L,k} = \left| \frac{\Delta p_k}{q_k} \right|, \tag{2.7}$$

where k is the Fourier mode, and Δp_k and q_k are the complex Fourier coefficients of the pressure drop $\Delta p(t) = \sum_{k=-M}^{M} \Delta p_k \exp\left(\frac{2\pi i k t}{T}\right)$ and volumetric flow rate $Q(t) = \sum_{k=-M}^{M} q_k \exp\left(\frac{2\pi i k t}{T}\right)$, respectively. The flow-rate coefficients $q_k = \sum A_j c_{j,k}$ are computed as Eqs 2.1 and 2.4, while $\Delta p(t)$ is computed as the difference between the area-weighted average pressure at the FM, $\bar{p}_{z=0}(t)$, and at a plane 2.5 cm caudal to the FM $\bar{p}_{z=-2.5}(t)$, such that

$$\Delta p(t) = \bar{p}_{z=-2.5} - \bar{p}_{z=0}. \tag{2.8}$$

The piecewise-linear curve of $Z_{L,k}$ in the frequency domain ($f = k/T$) is then integrated over 1-8 Hz to obtain the integrated longitudinal impedance.

3 Results

3.1 PC-MRI measurements: qualitative analysis

Cerebellar tonsillar motion and cervical CSF flow were characterized using the cardiac-gated PC-MRI measurements at three imaging planes (FM, C1–C2 or C2–C3, and C3–C4). For brevity, visualizations of the results are presented for representative subjects 3 and 6. The corresponding figures for the remaining subjects are provided in Appendix A.

We begin by examining qualitative characteristics of subject 3. The sagittal MRI in Figure 3a illustrates the cerebellar tonsillar herniation and the locations of the PC-MRI acquisition planes for this subject. Figure 3b shows the spatially averaged tonsillar velocity at the FM throughout the cardiac cycle. Preoperatively, the tonsils move in the caudal direction over a shorter duration and at a higher speed than they move in the rostral direction. Effectively, the tonsils rapidly displace downward while their cranial recovery is slower, a characteristic that has been reported in previous CM-I studies [25]. The cervical CSF flow rate waveforms shown in Figure 3c are approximately in phase with the tonsillar motion at the FM and exhibit a similar rapid caudal phase and slower rostral recovery. Figure 3d presents the instantaneous CSF velocity fields at the C3–C4 level, where the PC-MRI-based inlet boundary condition is prescribed in subsequent CFD simulations. The velocity fields are shown at three selected instances during the cardiac cycle: peak rostral flow, flow reversal, and peak caudal flow. Note that flow reversal is defined as the instance where the flow direction changes from rostral to caudal flow, and a different color scale (-5 to 5 cm/s) is used here to better resolve the low velocities that occur at this instance. As expected, CSF at the instance of peak caudal flow exhibits a larger velocity magnitude than at peak rostral flow. The preoperative CSF flow is anteriorly dominant, with high-velocity jets in the anterior region. During flow reversal, bidirectional flow is observed, with the anterior jets maintaining rostral flow while the rest of the CSF has already begun transitioning to caudal, as seen in previous studies [16]. Nozaleda et al.

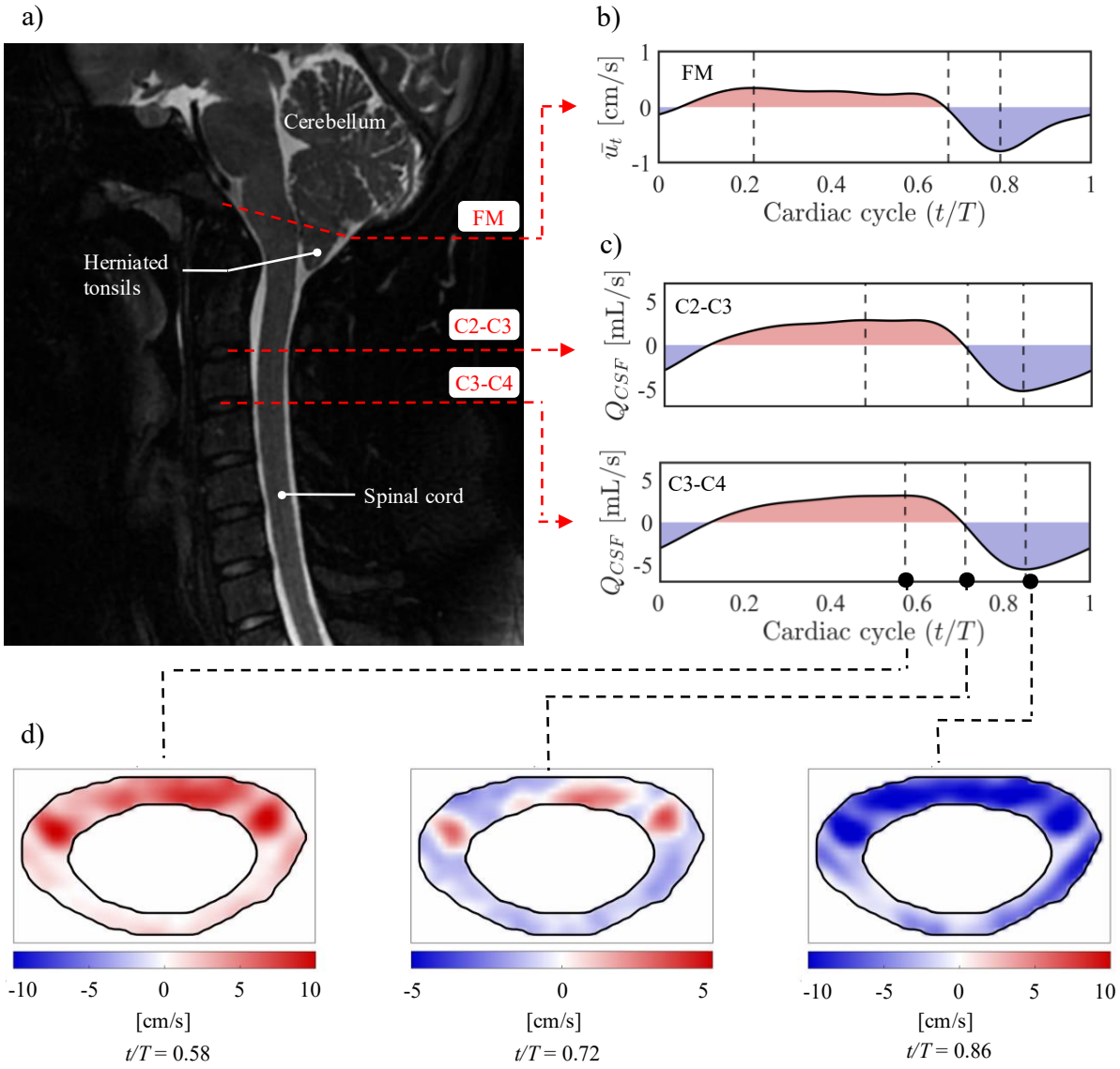

Figure 3. Preoperative MRI data for subject 3. a) Sagittal MRI. b) Tonsillar velocity at the FM. c) CSF flow rate at C2–C3 and C3–C4 throughout a cardiac cycle. Dashed lines indicate peak caudal flow, peak rostral flow, and flow reversal. d) Instantaneous velocity fields at these instances. At flow reversal, a narrower color scale (-5 to 5 cm/s) is used to resolve low velocities.

proposed that denticulate ligaments may act as an anterior-posterior flow separation barrier, contributing to distinct flow patterns in each region. This separation may be particularly relevant in CM-I, where tonsillar obstruction of the posterior CSF space at the craniocervical junction may exaggerate anterior-posterior flow differences.

A similar qualitative analysis is performed for subject 6. Figure 4a demonstrates the presence of a syrinx at the lower cervical levels. Unlike subject 3, Figure 4b shows that the tonsils move in the

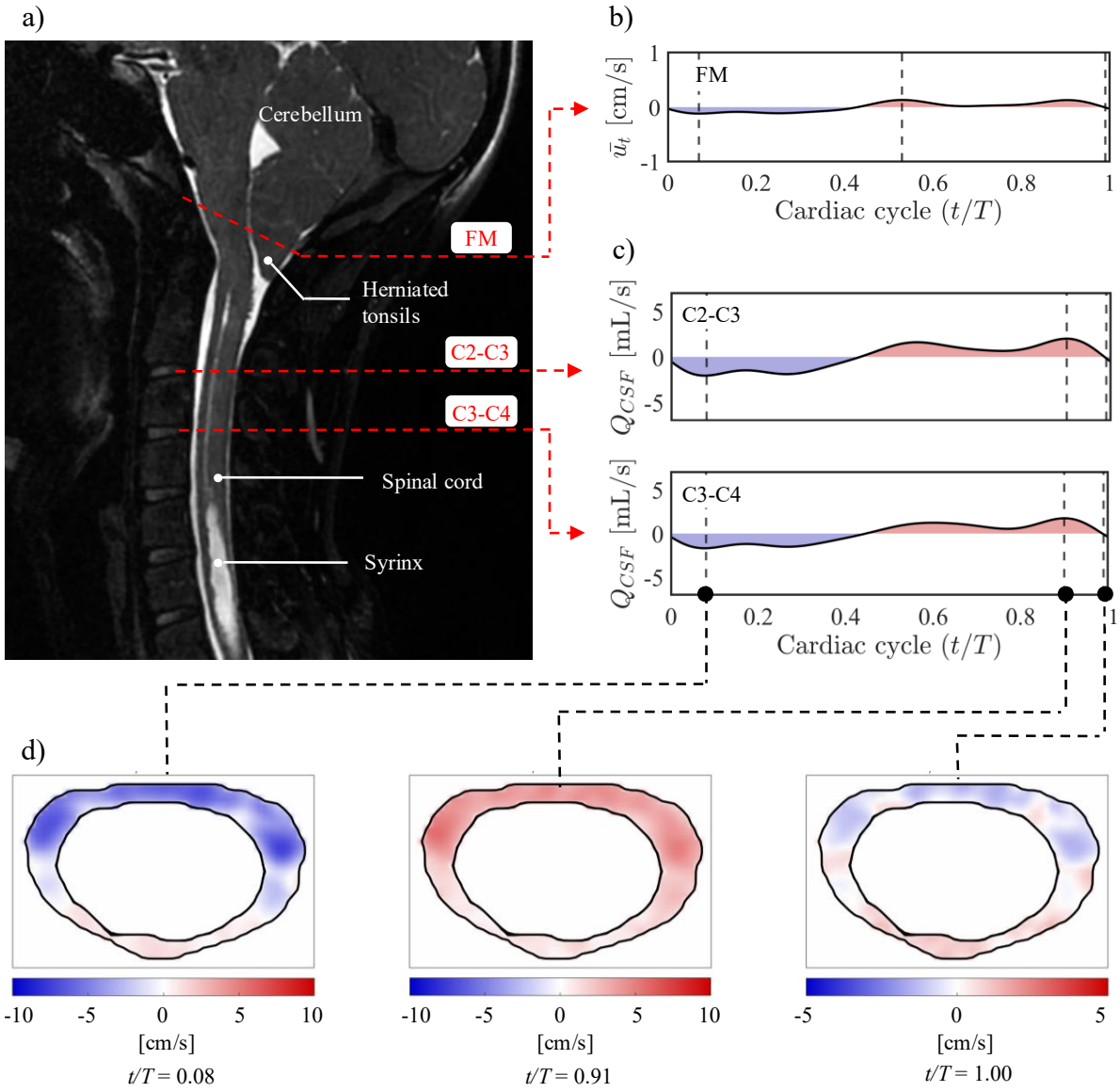

Figure 4. Preoperative MRI data for subject 6. a) Sagittal MRI. b) Tonsillar velocity at the FM. c) CSF flow rate at C2–C3 and C3–C4 throughout a cardiac cycle. Dashed lines indicate peak caudal flow, peak rostral flow, and flow reversal. d) Instantaneous velocity fields at these instances. At flow reversal, a narrower color scale (-5 to 5 cm/s) is used to resolve low velocities.

caudal and rostral directions with comparable magnitudes and durations. While the caudal phase remains slightly shorter in duration, similar to subject 3, the peak rostral velocity marginally exceeds the peak caudal velocity, opposite to the trend observed in subject 3. Nonetheless, in Figure 4c, the CSF flow rate waveforms remain approximately in phase with the tonsillar motion at the FM. The instantaneous CSF velocity fields in Figure 4d show less pronounced anterior jets than subject 3, corresponding to the overall

lower magnitudes in both CSF and tonsillar velocity that subject 6 exhibits. A different flow reversal pattern is also observed, as the anterior CSF transitions to caudal flow while the posterior CSF remains rostral, further demonstrating anterior-posterior differences in CSF flow.

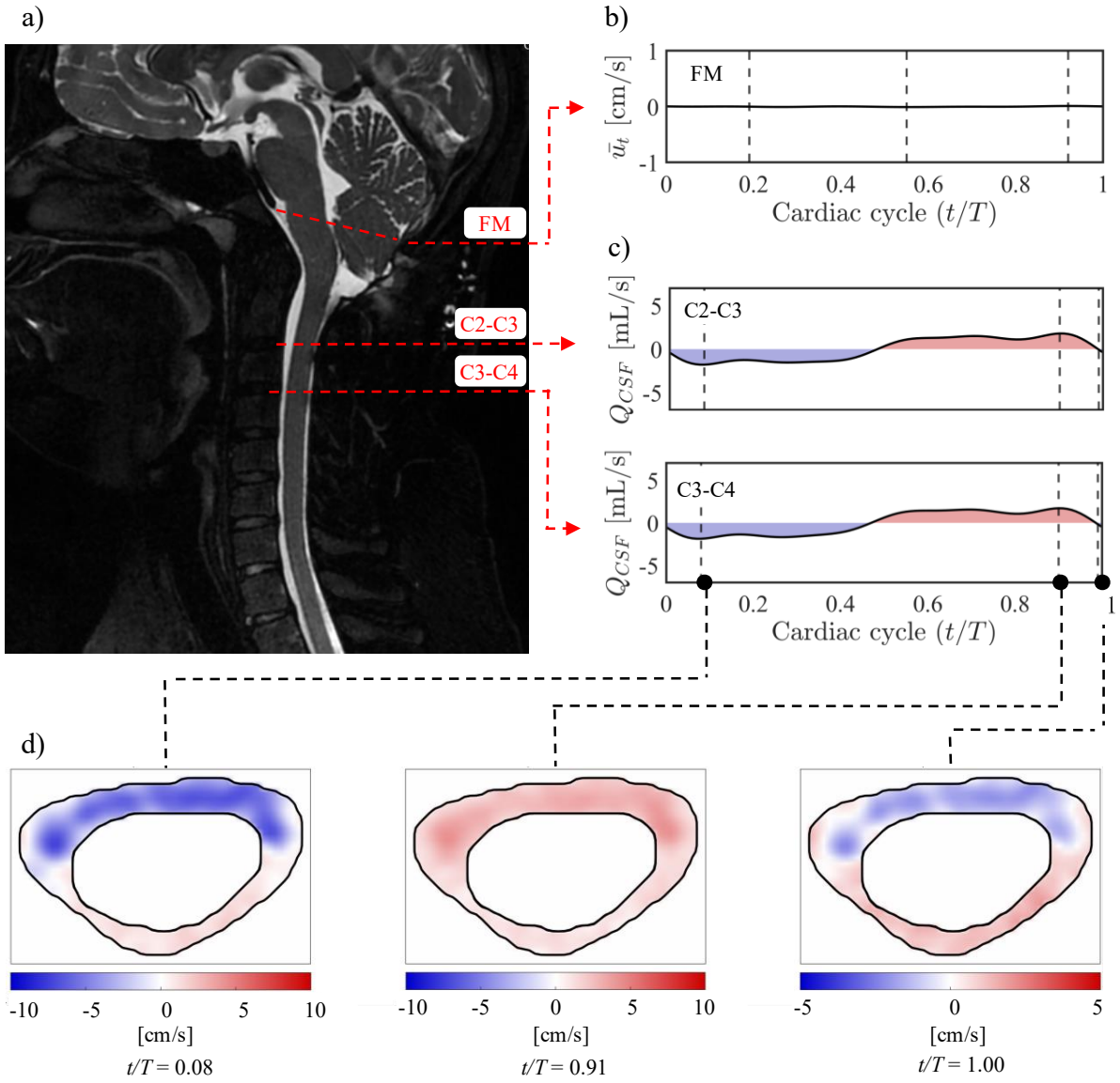

Figure 5. Postoperative MRI data for subject 3. a) Sagittal MRI. b) Tonsillar velocity at the FM. c) CSF flow rate at C2–C3 and C3–C4 throughout a cardiac cycle. Dashed lines indicate peak caudal flow, peak rostral flow, and flow reversal. d) Instantaneous velocity fields at these instances. At flow reversal, a narrower color scale (-5 to 5 cm/s) is used to resolve low velocities.

The corresponding postoperative PC-MRI data for subject 3 is visualized in Figure 5. Anatomical changes are evident in Figure 5a, where the cerebellar tonsils exhibit reduced herniation, appear more

round, and assume a more posterior orientation, consistent with previous CM-I studies [26]. Following surgical decompression, many of the preoperative abnormalities associated with tonsillar motion and CSF flow tend to normalize toward patterns observed in healthy subjects [27, 28]. As shown in Figure 5b, postoperative tonsillar motion at the FM is substantially reduced. Figure 5c shows a decrease in the magnitude of cervical CSF flow, and the rostral and caudal flow phases become comparable in both duration and magnitude. Unlike the rapid caudal displacement and slower rostral recovery observed preoperatively, the CSF maintains a more balanced flow in each direction. In Figure 5d, posterior CSF appears to maintain rostral flow throughout the cardiac cycle. However, there is a significant reduction in the anterior high-velocity jets, consistent with the reduction in both CSF and tonsillar velocities, and the overall velocity distribution appears more uniform. It is worth noting that for subject 3, the postoperative CSF flow waveforms appear out of phase with their preoperative counterparts, likely reflecting an MRI system software upgrade (to GE MR30.1) that occurred between the preoperative and postoperative acquisitions. Postoperative PC-MRI visualizations for subject 6 are presented in Figure 6, as both preoperative and postoperative scans for this subject were acquired after the software upgrade, allowing a more direct comparison of the flow waveforms.

Many postoperative observations for subject 6 are consistent with those of subject 3. Figure 6a displays similar changes in tonsillar shape and orientation, and Figure 6b demonstrates significant reduction in tonsillar motion. Unlike subject 3, Figure 6c shows a postoperative increase in the magnitude of CSF flow. The magnitudes and durations of CSF flow remain balanced in the caudal and rostral directions. Contrasting their preoperative pattern, lower cervical CSF flow appears to be significantly out of phase with tonsillar motion at the FM. In Figure 6d, the posterior CSF flow maintains a rostral direction throughout the cardiac cycle following surgical decompression, consistent with subject 3. Most subjects in the cohort exhibit similar rostral posterior flow, shown in Appendix A.

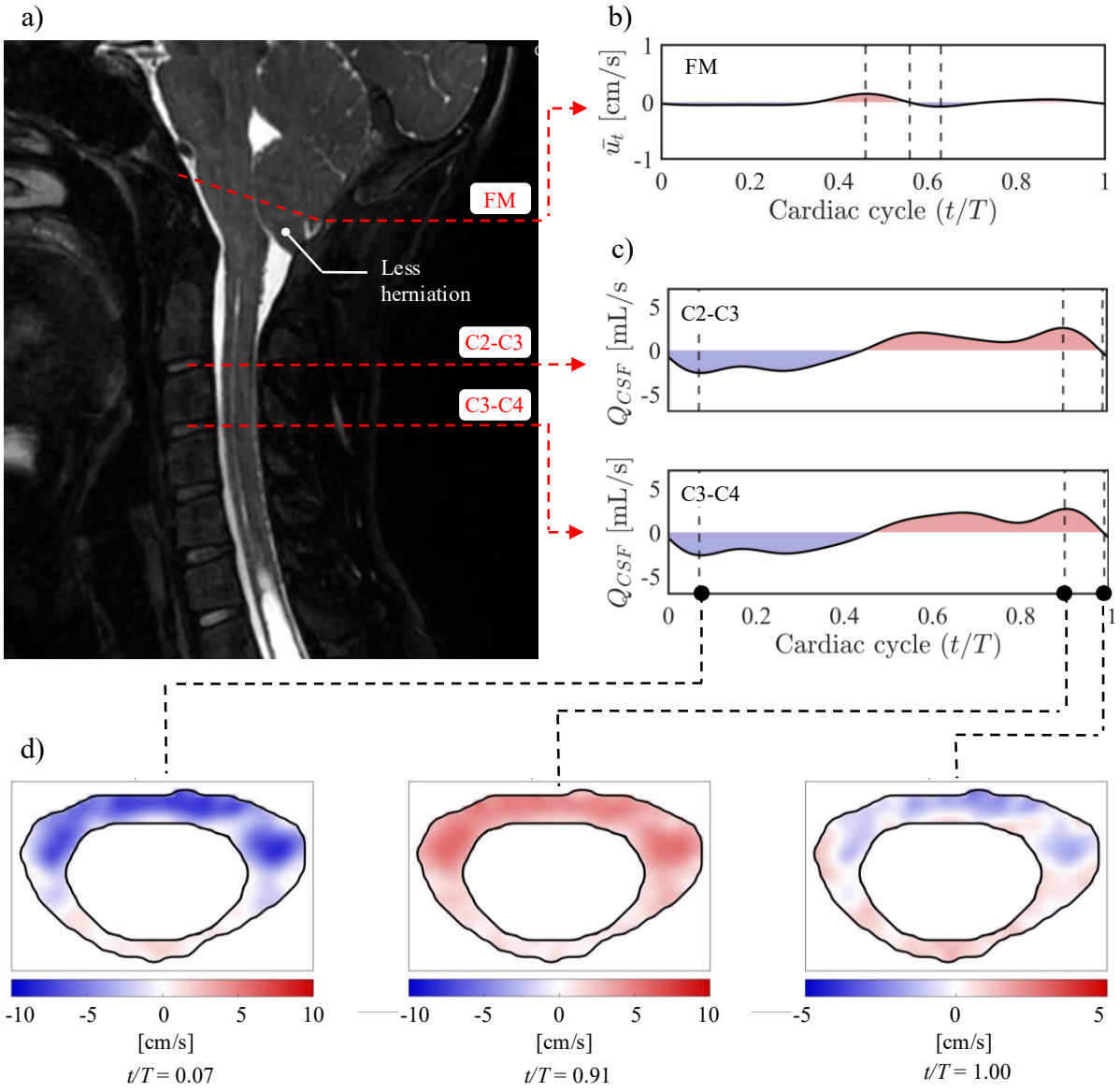

Figure 6. Postoperative MRI data for subject 6. a) Sagittal MRI. b) Tonsillar velocity at the FM. c) CSF flow rate at C2–C3 and C3–C4 throughout a cardiac cycle. Dashed lines indicate peak caudal flow, peak rostral flow, and flow reversal. d) Instantaneous velocity fields at these instances. At flow reversal, a narrower color scale (-5 to 5 cm/s) is used to resolve low velocities.

3.2 PC-MRI measurements: quantitative analysis

3.2.1 Tonsillar motion

To quantify the qualitative observations above, Table 4 summarizes the PC-MRI-derived metrics describing cerebellar tonsillar motion at the FM level for all subjects. We first examine the preoperative measurements for subject 3 in Table 4a. The peak caudal and rostral tonsillar velocities demonstrate

significant tonsillar motion ($u^{-}_{t,max} = 0.79$ cm/s and $u^{+}_{t,max} = 0.34$ cm/s, respectively). Here, the peak caudal tonsillar velocity is over twice as large as the rostral ($u^{-}_{t,max}/u^{+}_{t,max} = 2.21$). In addition, caudal displacement occurs for only 38% of the cardiac cycle ($\Delta t/T = 0.38$), while the rostral phase occurs for 62% of the cardiac cycle. These values are consistent with the rapid downward displacement and slower rostral recovery of the tonsils observed qualitatively. Similar preoperative trends are observed throughout the cohort, where most subjects present a high peak caudal-to-rostral velocity ratio. Subjects 6 and 7 are the exception, as their peak rostral velocities exceed their caudal counterpart ($u^{-}_{t,max}/u^{+}_{t,max} = 0.82$ and 0.87, respectively). However, all subjects maintain a shorter caudal duration than rostral.

Table 4. Tonsillar motion metrics at the FM from cardiac-gated PC-MRI. Tonsillar descent z is measured from the FM (McRae line) to the inferior tonsil tip. Δz is the total displacement per cardiac cycle. $u_{t,max}$ denotes peak spatially-averaged caudal (-) and rostral (+) velocities, with ratio (-)/(+). The caudal peak instance within the caudal phase is $t_{peak}/\Delta t$, and the duration of the caudal phase is $\Delta t/T$.

a) Preoperative

Subject	z [mm]	Δz [mm]	$u_{t,max}$ [cm/s]			Caudal Phase	
			(-)	(+)	(-)/(+)	$t_{peak}/\Delta t$	$\Delta t/T$
1	18.90	1.41	0.56	0.25	2.21	0.40	0.29
2	20.57	1.86	0.70	0.28	2.55	0.31	0.31
3	8.25	1.98	0.79	0.34	2.31	0.34	0.38
4	17.25	N/A	N/A	N/A	N/A	N/A	N/A
5	9.15	0.55	0.14	0.10	1.33	0.23	0.43
6	12.08	0.36	0.10	0.12	0.82	0.17	0.44
7	6.95	0.56	0.12	0.14	0.87	0.55	0.46

b) Postoperative

Subject	z [mm]	Δz [mm]	$u_{t,max}$ [cm/s]			Caudal Phase	
			(-)	(+)	(-)/(+)	$t_{peak}/\Delta t$	$\Delta t/T$
1	13.00	0.08	0.02	0.03	0.70	0.82	0.39
2	15.80	0.35	0.13	0.12	1.11	0.27	0.39
3	6.27	0.02	0.01	0.02	0.57	0.51	0.59
4	11.21	1.58	0.32	0.22	1.44	0.15	0.45
6	6.50	0.34	0.10	0.15	0.55	0.40	0.58

Post-surgical changes in tonsillar motion are shown in Table 4b. For subject 3, tonsillar velocity is significantly reduced ($u^{-}_{t,max} = 0.010$ cm/s and $u^{+}_{t,max} = 0.017$ cm/s), and the peak caudal-to-rostral tonsillar velocity decreases ($u^{-}_{t,max}/u^{+}_{t,max} = 0.57$). The caudal duration increases to 59% of the cardiac

cycle ($\Delta t/T = 0.59$). These changes are consistent throughout the cohort, with many subjects exhibiting reduced tonsillar velocities and a peak caudal-to-rostral ratio that shifts closer to unity after surgery. Again, subject 6 is the exception, as the reduction in tonsillar motion is considerably smaller than the remainder of the cohort, and the peak caudal-to-rostral ratio shifts further from unity postoperatively. For all subjects, the duration of the caudal phase increases and becomes comparable to that of the rostral phase. These quantitative measurements represent the more balanced bidirectional tonsillar motion observed qualitatively following decompression.

The maximum distance of tonsillar herniation below the FM, z, is also reported. Following surgical decompression, the degree of tonsillar herniation is reduced for all subjects, with reductions ranging from around 23–46% across the cohort, consistent with previous CM-I studies [26]. Tonsillar displacement during the cardiac cycle, Δz, is generally greater preoperatively than the reported values for healthy subjects ($\simeq 0.43$ mm) [29]. Postoperatively, tonsillar displacement decreases substantially, with reductions ranging from around 81-99% for most subjects. In subject 6, tonsillar displacement decreases by only around 6%, likely related to the already small preoperative tonsillar displacement of this patient.

3.2.2 CSF flow

PC-MRI-derived metrics describing CSF flow at the lower cervical levels are summarized in Table 5. We first examine the preoperative measurements in Table 5a for subject 3. At both the C2–C3 and C3–C4 levels, the peak caudal CSF flow rate is nearly twice the peak rostral flow rate (Q^{-}_{max}/Q^{+}_{max} = 1.85 and 1.75, respectively), consistent with the asymmetry observed in tonsillar motion at the FM. Caudal CSF flow at C2–C3 and C3–C4 occurs for 40% and 41% of the cardiac cycle, respectively, comparable to the duration of caudal tonsillar motion. Similarly, the timing of peak caudal CSF flow within the caudal phase ($t_{peak}/\Delta T = 0.35$ and 0.36 at C2–C3 and C3–C4, respectively) is consistent with that of peak caudal tonsillar motion at the FM ($t_{peak}/\Delta T = 0.38$), supporting the qualitative observation that preoperative cervical CSF flow is in phase with tonsillar motion at the FM. Most subjects display similar behavior, following the tonsillar motion trends.

We now examine postoperative changes in cervical CSF flow in Table 5b. For subject 3, the CSF flow magnitude decreases postoperatively. While some subjects in the cohort follow this trend, others exhibit a postoperative increase in CSF flow, consistent with previous studies reporting variable changes

Table 5. CSF flow metrics at two lower cervical planes derived from cardiac-gated PC-MRI. Q_{max} represents the peak flow rate in the caudal (-) and rostral (+) directions, and their ratio is (-)/(+). The instance of peak caudal flow within the caudal phase is $t_{peak}/\Delta t$, and the duration of the caudal phase is $\Delta t/T$. The ratio of the peak to mean velocity at the systolic peak is $u_{peak}/|\bar{u}|$, and the stroke volume is V_s.

a) Preoperative

Subject	Location	Q_{max} [mL/s]			Caudal Flow Phase		$u_{peak}/\lvert\bar{u}\rvert$	V_s
		(-)	(+)	(-)/(+)	$t_{peak}/\Delta t$	$\Delta t/T$		
1	C1-C2	2.96	1.05	2.82	0.51	0.23	2.27	0.41
	C3-C4	4.27	1.78	2.40	0.44	0.25	1.85	0.63
2	C1-C2	3.85	1.73	2.23	0.33	0.32	1.34	0.54
	C3-C4	4.19	1.80	2.33	0.34	0.32	1.80	0.60
3	C2-C3	5.25	2.83	1.85	0.35	0.40	2.36	0.84
	C3-C4	5.58	3.19	1.75	0.36	0.41	2.15	0.89
5	C2-C3	6.58	6.03	1.09	0.18	0.45	1.88	1.41
	C3-C4	4.12	4.56	0.90	0.15	0.51	2.05	1.11
6	C2-C3	2.07	2.01	1.03	0.19	0.44	2.37	0.39
	C3-C4	1.87	1.91	0.98	0.18	0.46	2.58	0.35
7	C2-C3	4.32	2.84	1.52	0.24	0.39	2.28	1.16
	C3-C4	5.38	2.97	1.81	0.27	0.36	2.49	1.17

b) Postoperative

Subject	Location	Q_{max} [mL/s]			Caudal Flow Phase		$u_{peak}/\lvert\bar{u}\rvert$	V_s
		(-)	(+)	(-)/(+)	$t_{peak}/\Delta t$	$\Delta t/T$		
1	C1-C2	3.46	3.31	1.04	0.19	0.42	1.86	0.67
	C3-C4	3.75	3.61	1.04	0.21	0.40	1.98	0.73
2	C2-C3	1.10	1.97	0.55	0.12	0.60	2.94	0.15
	C3-C4	1.91	2.19	0.87	0.19	0.44	2.26	0.29
3	C2-C3	1.79	1.81	1.01	0.17	0.49	2.12	0.41
	C3-C4	1.88	1.73	1.08	0.18	0.48	2.49	0.40
4	C2-C3	4.01	2.90	1.38	0.18	0.47	2.50	1.08
	C3-C4	3.87	2.84	1.36	0.18	0.49	2.17	1.08
6	C2-C3	2.61	2.57	1.01	0.17	0.46	2.44	0.53
	C3-C4	2.24	2.32	0.97	0.16	0.48	2.62	0.52

in CSF flow following surgical decompression [30–32]. Nonetheless, peak caudal CSF flow becomes comparable to peak rostral CSF flow (Q^{-}_{max}/Q^{+}_{max} = 1.01 and 1.08 at C2–C3 and C3–C4, respectively), and the duration of caudal CSF flow increases ($\Delta t/T = 0.49$ and 0.48 at C2–C3 and C3–C4, respectively), trends that align with tonsillar behavior and generally occur throughout the cohort. However, for subject

3, while peak caudal tonsillar motion occurs later within the caudal phase ($t_{peak}/\Delta T = 0.51$), peak caudal CSF flow occurs much earlier ($t_{peak}/\Delta T = 0.17$ and 0.18 at C2-C3 and C3-C4, respectively). Unlike tonsillar motion, where peak caudal motion occurs earlier for some patients and later for others following surgery, this shift to an earlier peak caudal flow of CSF is consistent throughout the cohort, supporting the observation that postoperative cervical CSF flow becomes out of phase with tonsillar motion.

The ratio of peak to mean velocity at the systolic peak $u_{peak}/|\bar{u}|$ was included as a descriptive measure of the spatial variability of the velocity field. Although this ratio increased in several postoperative cases, the subjects often exhibited a reduction in the mean velocity magnitude. Consequently, changes in $u_{peak}/|\bar{u}|$ reflect variations in both the spatial distribution of the velocity field and the overall flow magnitude, and should not be interpreted as a direct measure of spatial uniformity alone. The qualitative visualizations of the velocity fields may provide a better representation of postoperative changes in the spatial distribution of CSF flow. Additionally, CSF stroke volume across the lower cervical levels, V_s, showed variable responses across the cohort. For subject 3, the stroke volume decreases following decompression, whereas subject 6 exhibits a postoperative increase. This patient-specific variability is observed throughout the remainder of the cohort, with no consistent direction of postoperative change. Direct comparison with previous studies is limited, as few studies have reported pre- and postoperative CSF stroke volume at comparable cervical levels.

3.3 CFD: CSF pressure dynamics

To complement the PC-MRI measurements, pressure-based metrics obtained from the CFD simulations are presented. Note that preoperative simulations and corresponding metrics are not computed for subject 1 due to unavailable T2-weighted images and subject 4 due to unavailable PC-MRI measurements. Figure 7 shows the evolution of the longitudinal pressure drop, Δp, between the FM and an axial plane 2.5 cm below, as defined in Eq 2.8. The preoperative cases in Figure 7a demonstrate inter-subject variability in the shape and magnitude of the pressure-difference waveforms, whereas the postoperative cases in Figure 7b exhibit more similar pressure drop evolutions across subjects.

The maximum pressure difference, $\max(\Delta p)$, for each subject is listed in Table 6. Preoperative values ranged from 7.76 to 14.36 Pa, on the same order of magnitude as values previously reported for

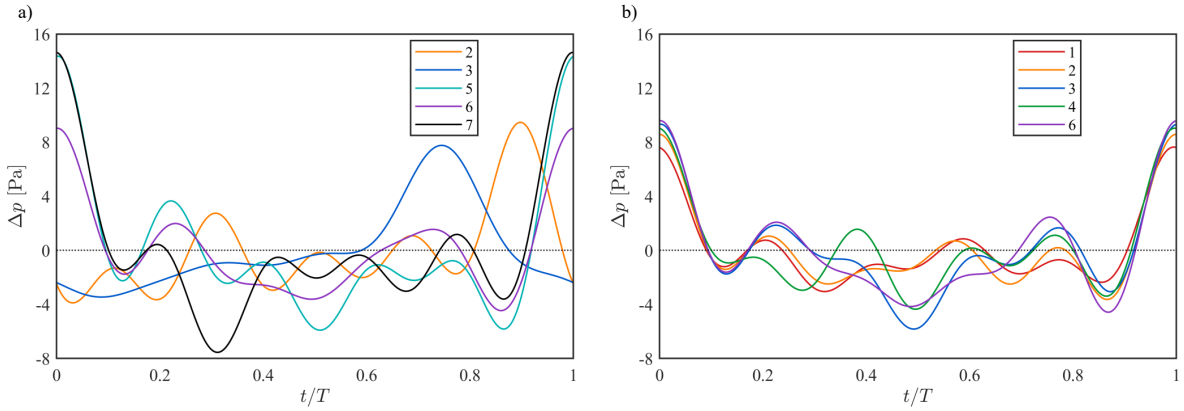

Figure 7. Evolution of the longitudinal pressure difference Δp (Eq 2.8) over the cardiac cycle for the a) preoperative and b) postoperative cases.

CM-I patients. Martin et al. reported maximum pressure differences of 11.73 Pa (0.088 mmHg) for one patient (CP1) and 18.13 Pa (0.136 mmHg) for the other (CP2) [18], while Nozaleda et al. reported a maximum pressure difference of 6.1 Pa in their most PC-MRI-informed model [16]. Nozaleda et al. partially attributed their reportedly lower pressure difference to the lower PC-MRI-measured flow rates prescribed in their model relative to those of Martin et al. In the present cohort, however, differences in peak flow rate and $\max(\Delta p)$ across subjects did not exhibit a consistent relationship, indicating that differences in flow magnitude alone do not fully explain the observed pressure response. Differences in craniocervical geometry contributes to CSF pressure dynamics, as reflected in the following longitudinal impedance discussion. Postoperatively, $\max(\Delta p)$ had a smaller range of values than the preoperative cases, from 7.64 to 9.59 Pa. Compared to their preoperative counterparts, the postoperative maximum pressure difference showed no consistent directional change, increasing in some subjects and decreasing in others, as found in previous works. For instance, Martin et al. reported a postoperative increase to 12.93 Pa (0.097 mmHg) for CP1, whle CP2 showed a decrease to 13.73 Pa (0.103 mmHg) [18].

To further characterize CSF pressure dynamics, longitudinal impedance, computed from the frequency-domain relationship between pressure drop and volumetric flow rate as described in Section 2.4, is also reported in Table 6. Preoperative values range from approximately 282 to 365 dyn/cm^5, comparable to results from previous studies. Martin et al. reported longitudinal impedance values of 440 and 335 dyn/cm^5 for CP1 and CP2, respectively [18], and Nozaleda et al. reported approximately 331 dyn/cm^5 in their most PC-MRI-informed model [16]. In addition, the preoperative longitudinal impedance for all

Table 6. Pressure-based metrics derived from CFD simulations. The maximum pressure drop between the FM and an axial plane 2.5 cm below is denoted as $\max(\Delta p)$. LI represents the integrated longitudinal impedance, as computed in Section 2.4.

	$\max(\Delta p)$ [Pa]		LI [dyn/cm^5]	
Subject	Preoperative	Postoperative	Preoperative	Postoperative
1	N/A	7.64	N/A	173.27
2	9.47	8.58	281.67	246.93
3	7.76	9.33	360.99	329.75
4	N/A	9.04	N/A	331.55
5	14.36	N/A	303.62	N/A
6	9.03	9.59	353.58	302.71
7	14.64	N/A	364.57	N/A

subjects is higher than values reported for healthy individuals ($\simeq 143-244$ dyn/cm^5 across previous studies) [18, 19, 33], consistent with reports of elevated longitudinal impedance in CM-I patients. Unlike the variable postoperative changes observed in $\max(\Delta p)$, longitudinal impedance values for all subjects decrease compared to their preoperative counterparts, with reductions ranging from approximately 9–14%. Martin et al. also reported postoperative decreases in longitudinal impedance, although reductions of approximately 20–30% were observed in their two patients [18]. Nonetheless, postoperative longitudinal impedance generally remains higher than values reported for healthy controls. Neither the maximum pressure difference nor longitudinal impedance exhibited a clear association with the PC-MRI-derived metrics evaluated in the present study or with the symptoms reported in Table 1. Similar variability has been reported previously, with longitudinal impedance found to correlate with some measures of CM-I severity but not others [33].

4 Discussion

The PC-MRI measurements suggest that posterior fossa decompression alters the relationship between cerebellar tonsillar motion and cervical CSF flow. Preoperatively, the rapid, caudal displacement of the tonsils and the closely-paralleled CSF behavior support Oldfield's hypothesis that piston-like tonsillar motion drives oscillatory CSF flow. Following decompression, the significant reduction in tonsillar motion likely reflects expansion of the SAS and reduced resistance to CSF flow at the craniocervical junction. Consequently, tonsillar motion may have less influence on CSF flow further down the spinal canal, reflected in the postoperative loss of synchrony between tonsillar motion and cervical CSF flow. One possible explanation is that restoration of a more patent SAS allows the intracranial pressure pulse to play a larger role in driving postoperative CSF flow, producing flow patterns that more closely resemble those of healthy individuals [34]. A potential implication of the altered temporal relationship between the cerebellar tonsils and CSF is its effect on fluid entrance into the spinal cord. Previous studies have suggested that the timing of CSF pulsations influences fluid transport through the perivascular spaces [8]. Although the MRI software upgrade prevented definitive assessment of the postoperative CSF waveform phase for some subjects, the timing metrics evaluated in the present study–including the duration of the caudal phase and the timing of peak caudal flow within the caudal phase–are less dependent on the absolute waveform phase and may provide preliminary evidence of temporal changes in CSF flow associated with surgical decompression.

The pressure-based CFD metrics provide further insight into the anatomical changes related to CM-I. Although the maximum longitudinal pressure difference did not exhibit a consistent change from the preoperative to postoperative cases, longitudinal impedance consistently decreased following decompression, reflecting reduced resistance to oscillatory CSF flow associated with craniocervical obstruction. Interestingly, despite variable intrasubject changes in $\max(\Delta p)$ following surgery, postoperative values exhibited less intersubject variability than preoperative values. This may reflect more similar hydrodynamic

conditions following decompression, although additional subjects would be required to establish whether this represents a consistent postoperative effect. Nevertheless, the lack of a clear relationship between these pressure-based markers and the PC-MRI metrics or clinical symptoms in this study suggests that the parameters evaluated here may only partially characterize the physiological changes associated with surgical decompression. Fully characterizing craniocervical obstruction and its influence on oscillatory CSF flow may therefore require complementary physiological markers. Future CFD studies could further investigate the relationship between CSF flow, pressure dynamics, and anatomical obstruction in CM-I to better explain inter-subject variability and their potential role in syrinx formation.

Other limtations of the present study should be noted. The relatively small cohort size restricts the generalizability of these findings to the broader CM-I population. Only one subject presented with a syrinx, and inclusion of more CM-I patients with syringomyelia may provide additional insight into the relationship between syrinx formation and the metrics evaluated in this study. As mentioned, the exclusion of anatomical structures may limit understanding of the spatial distribution of CSF flow in CM-I, and inclusion of denticulate ligaments in particular may help explain differences between anterior and posterior CSF flow characteristics. Finally, the CFD model treats the cerebellar tonsils as a rigid body and does not account for tissue deformation. Future CFD Chiari studies should incorporate fluid-structure interaction to better capture the effects of tonsillar deformation, which may provide further insight into CSF dynamics within the narrow region between the tonsils and the spinal cord.

A Additional PC-MRI Visualiztions

Figures **8.1–8.7** present the MRI visualizations for all other subjects in this cohort. Unless otherwise noted, each figure follows the same format: a) sagittal MRI showing the anatomy; b) tonsillar velocity at the FM; c) CSF flow rates at the lower cervical levels; d) instantaneous velocity fields at peak caudal flow, peak rostral flow, and flow reversal. At flow reversal, a narrower color scale (-5 to 5 cm/s) is used to better resolve low-magnitude velocities.

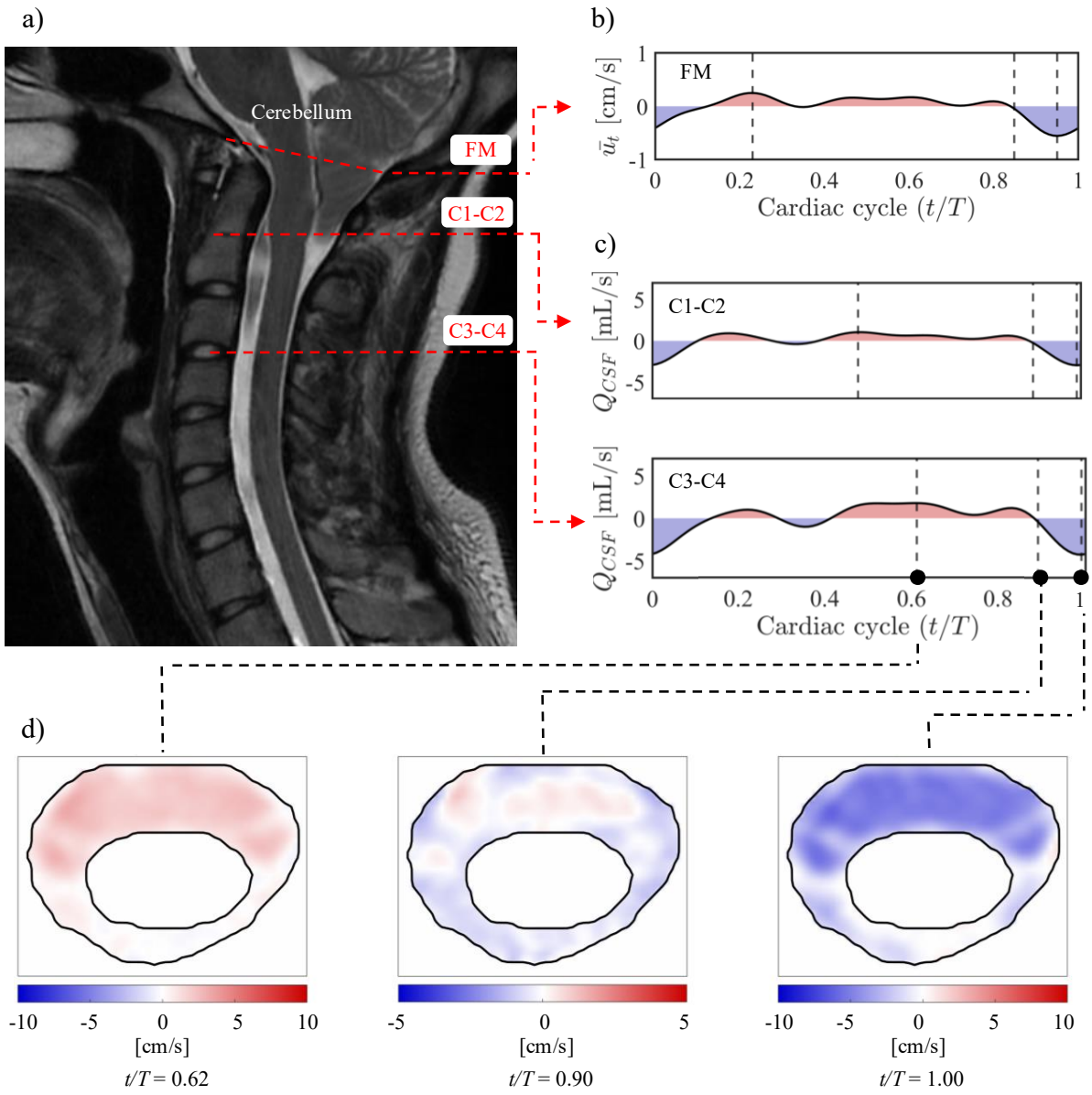

Figure 8.1. Preoperative MRI data for subject 1.

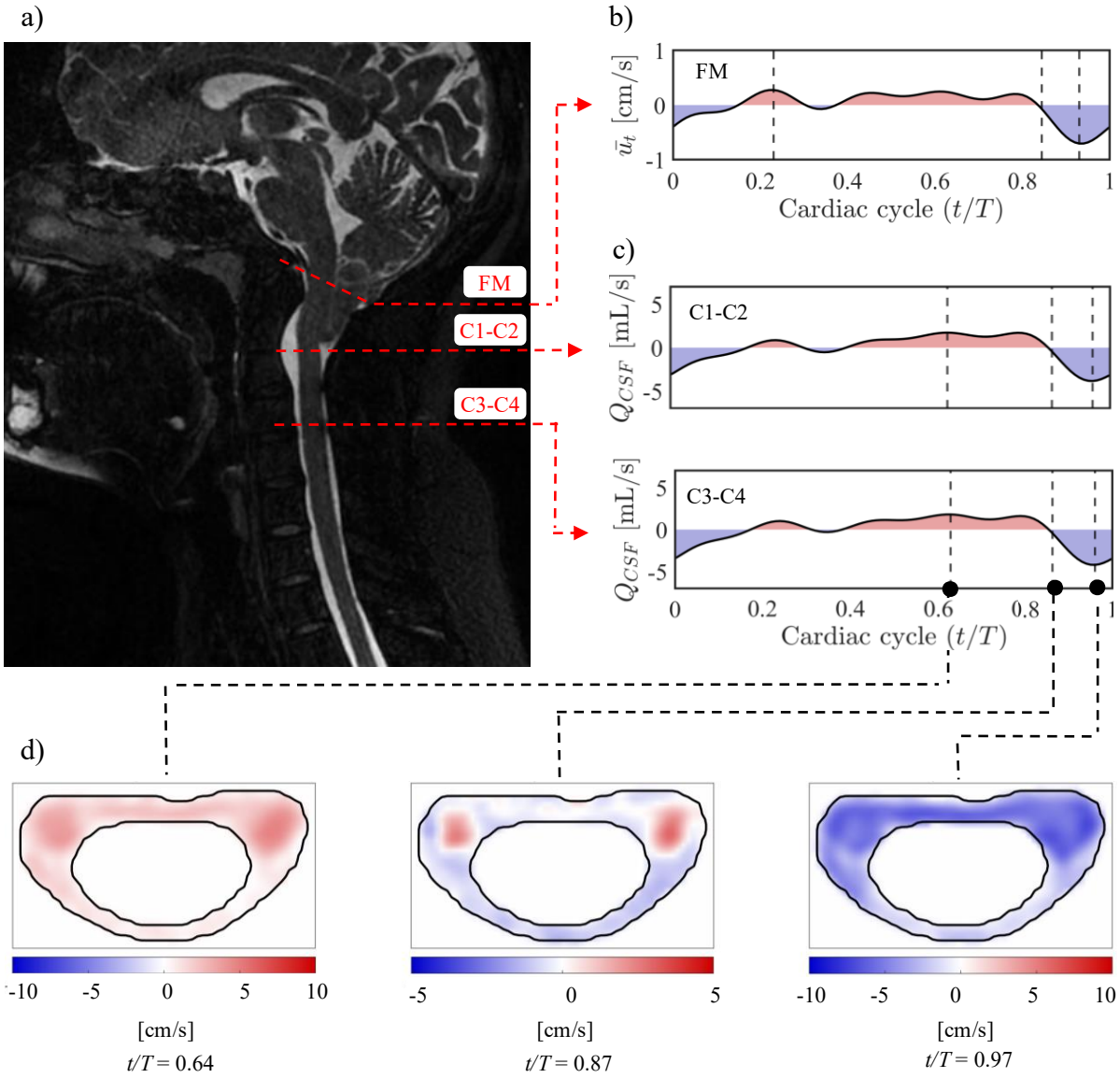

Figure 8.2. Preoperative MRI data for subject 2.

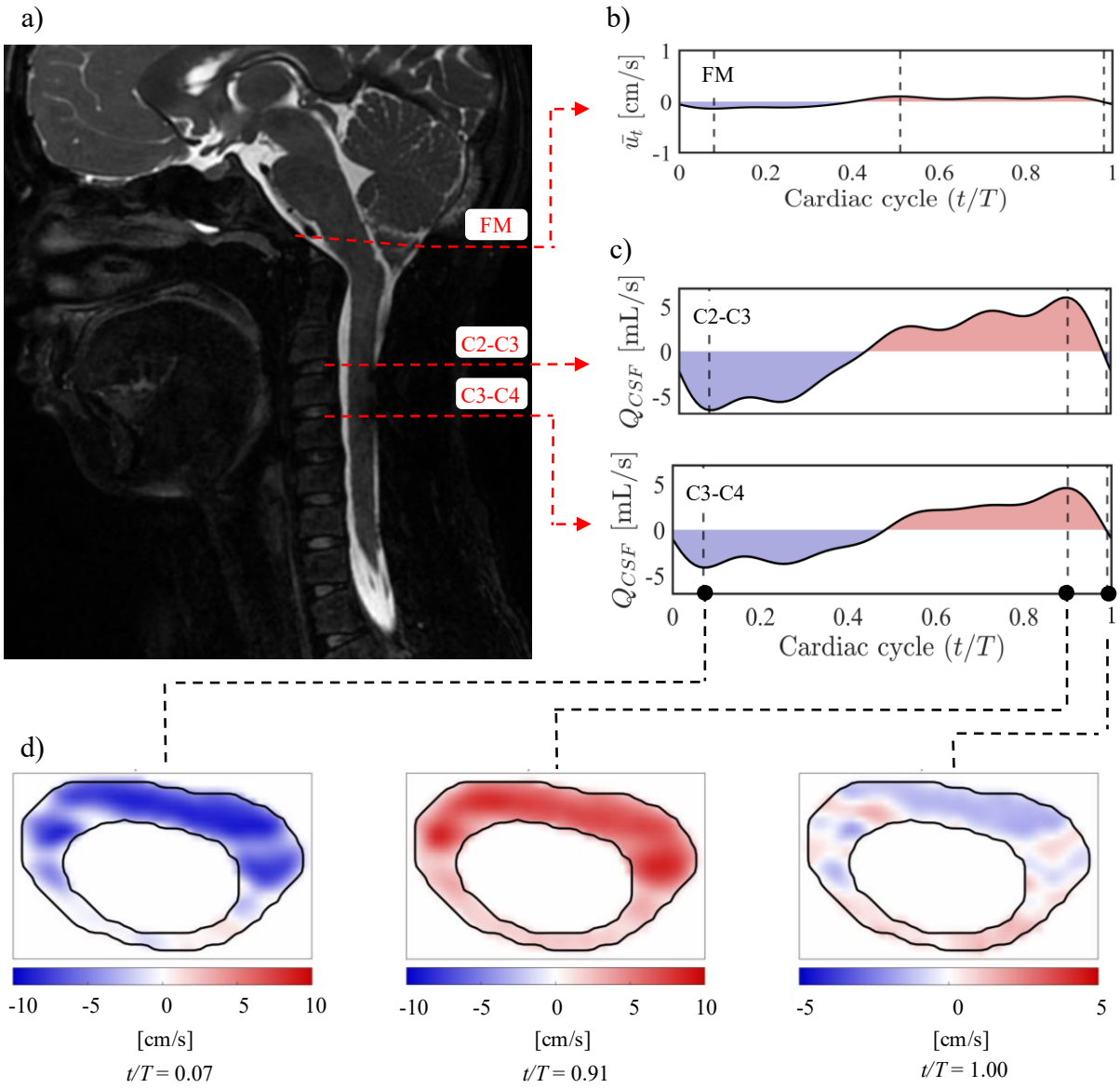

Figure 8.3. Overview of preoperative MRI data for subject 5.

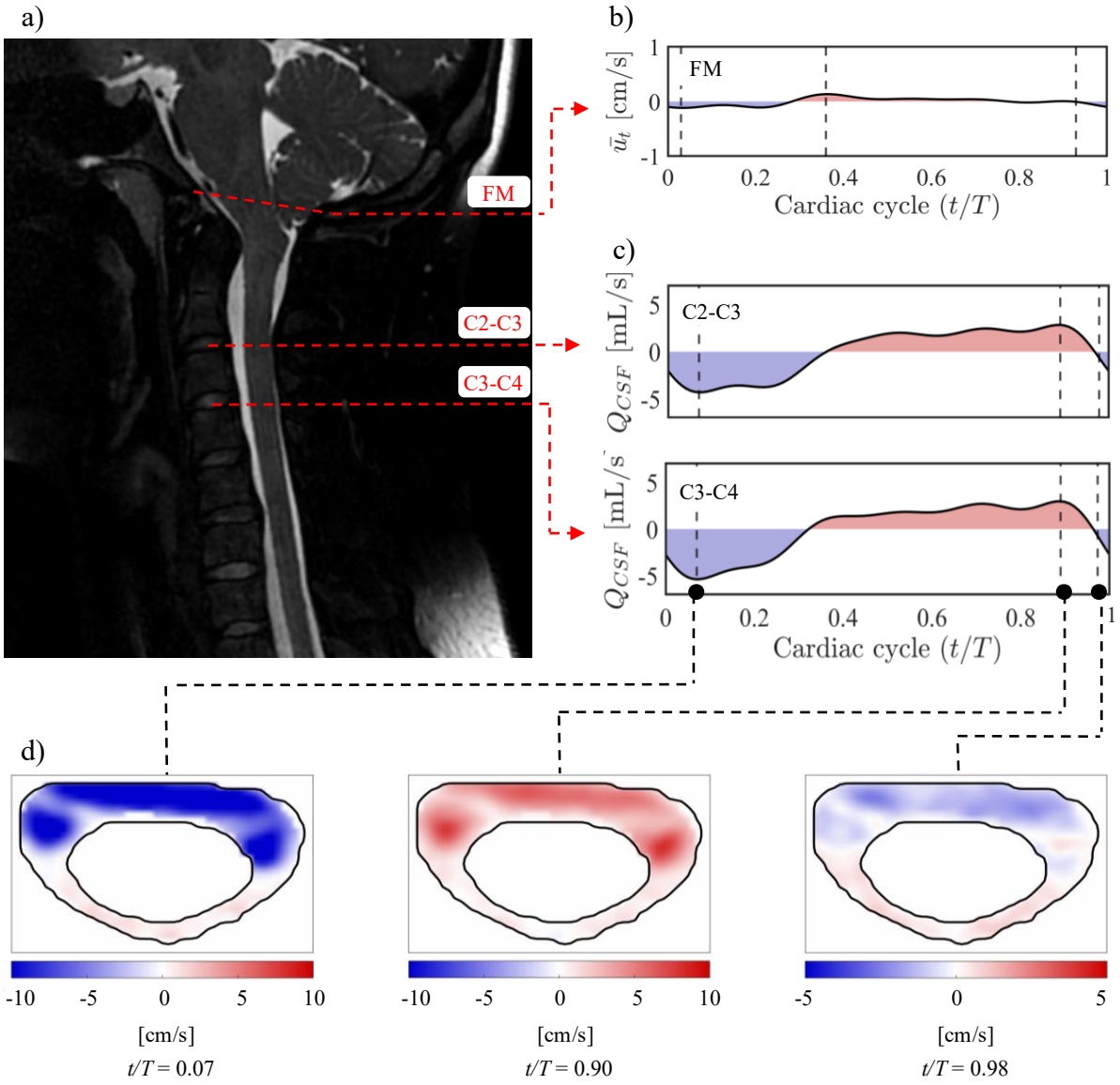

Figure 8.4. Preoperative MRI data for subject 7.

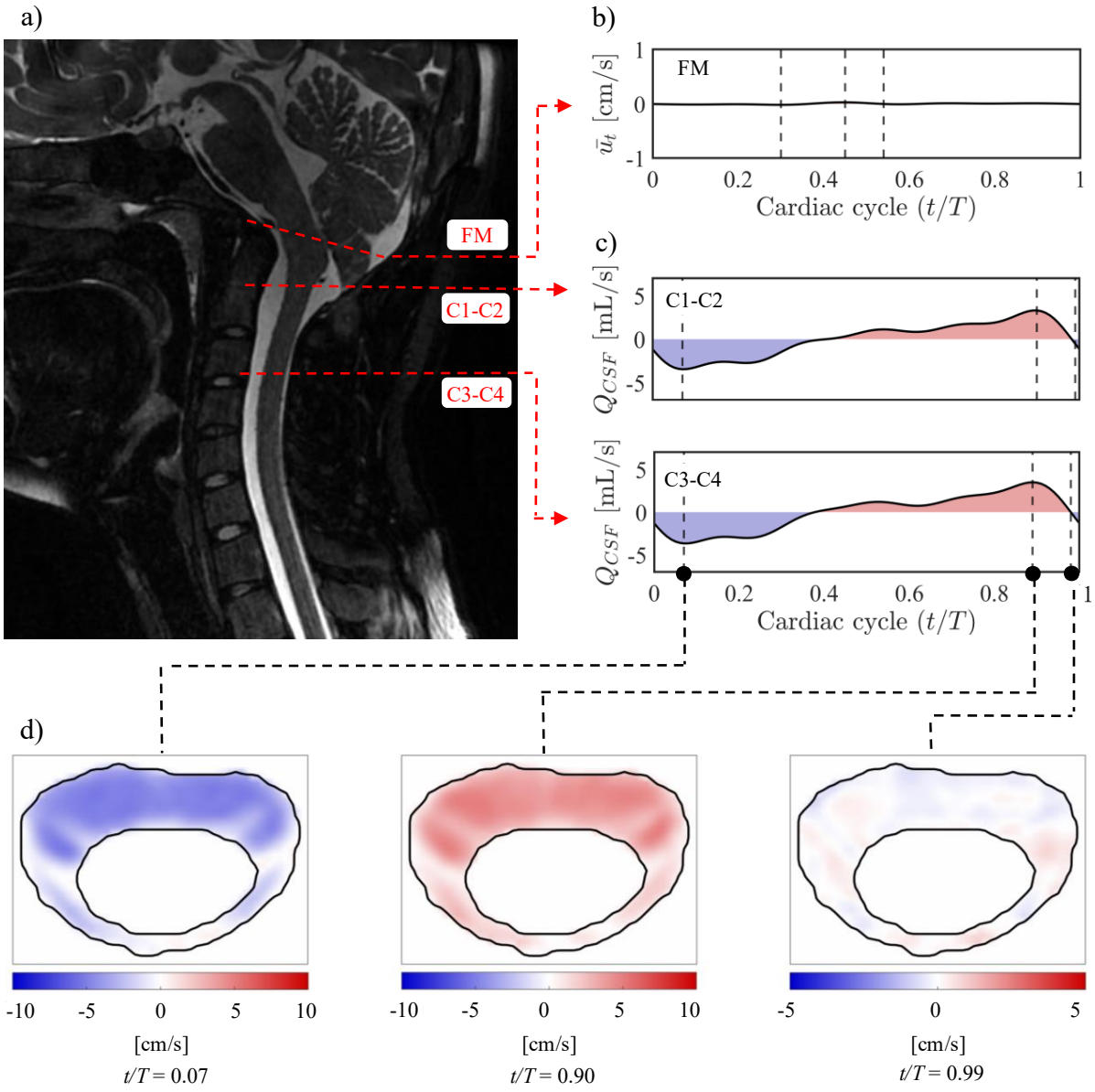

Figure 8.5. Postoperative MRI data for subject 1.

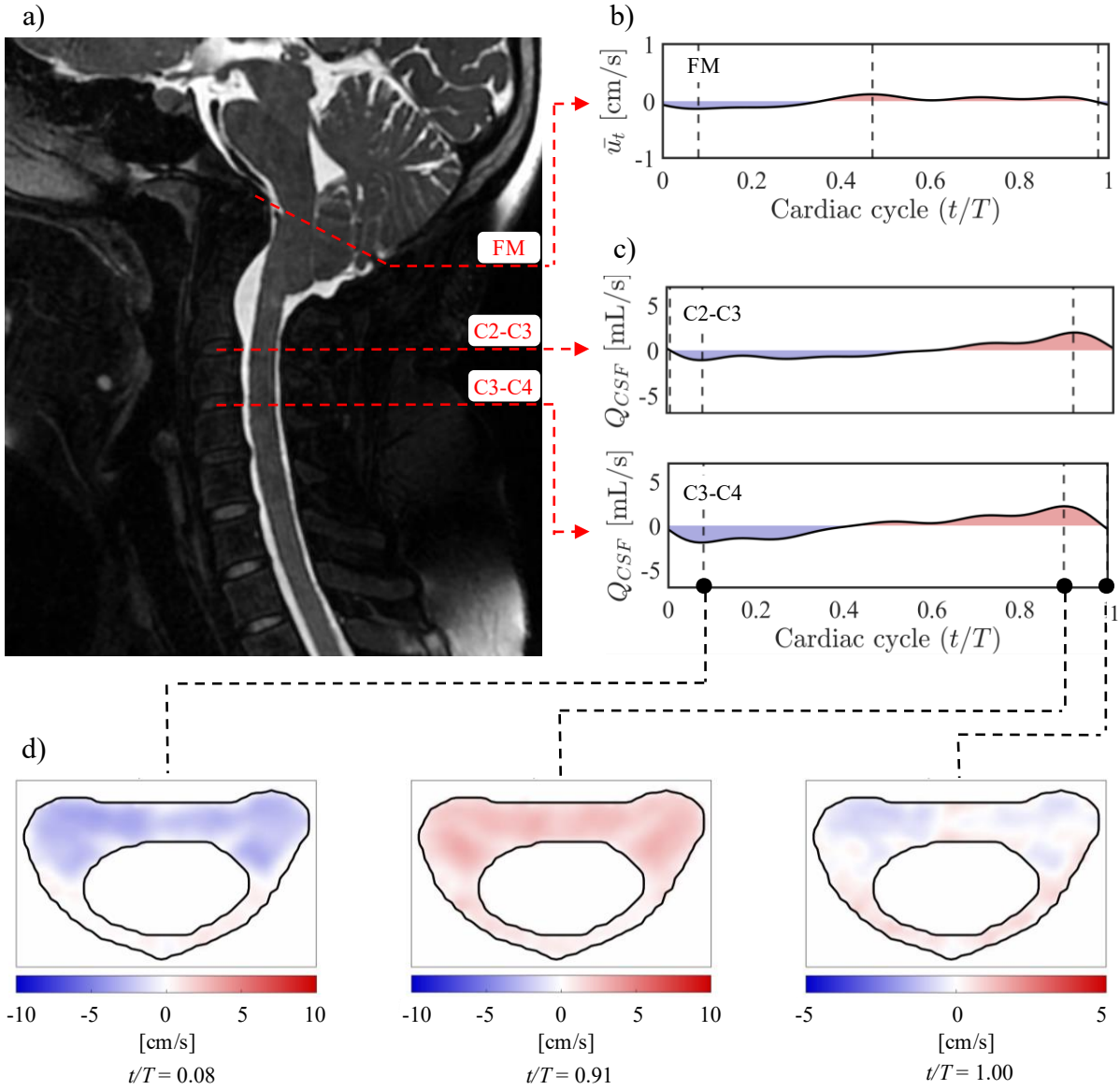

Figure 8.6. Postoperative MRI data for subject 2.

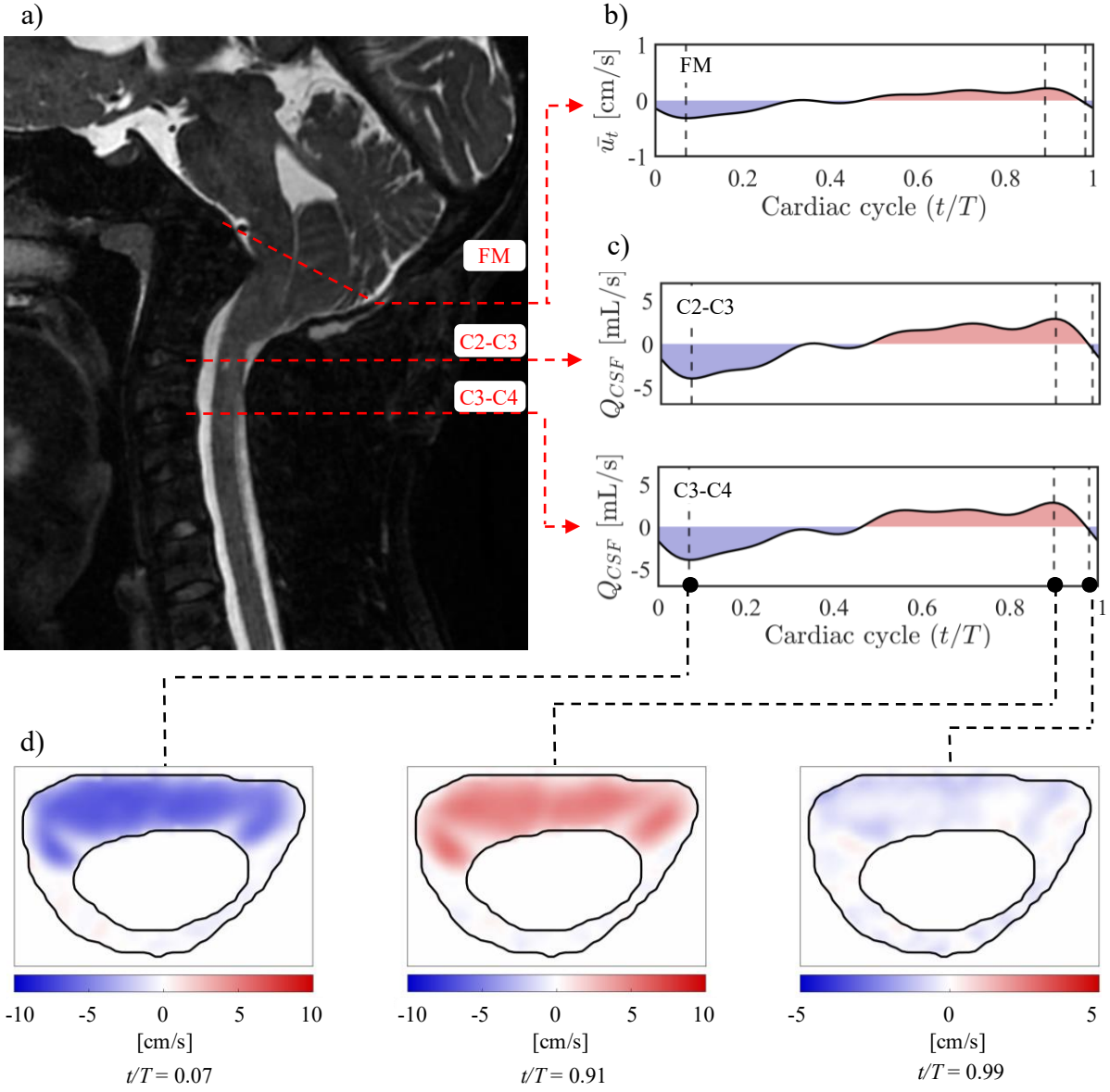

Figure 8.7. Postoperative MRI data for subject 4.

References

[1] M. Panigrahi, B. P. Reddy, A. Reddy, and J. Reddy, "Csf flow study in Chiari I malformation," *Child's Nervous System*, vol. 20, pp. 336–340, 2004.

[2] N. Shaffer, B. Martin, and F. Loth, "Cerebrospinal fluid hydrodynamics in Type I Chiari malformation," *Neurological Research*, vol. 33, no. 3, pp. 247–260, 2011.

[3] J. Klekamp, "The pathophysiology of syringomyelia: Historical overview and current concept," *Acta Neurochirurgica*, vol. 144, pp. 649–664, 2002.

[4] G. Pinna, F. Alessandrini, A. Alfieri, M. Rossi, and A. Bricolo, "Cerebrospinal fluid flow dynamics study in Chiari I malformation: Implications for syrinx formation," *Neurosurgical Focus*, vol. 8, no. 3, pp. 1–8, 2000.

[5] M. L. Rennels, T. F. Gregory, O. R. Blaumanis, K. Fujimoto, and P. A. Grady, "Evidence for a "paravascular" fluid circulation in the mammalian central nervous system, provided by the rapid distribution of tracer protein throughout the brain from the subarachnoid space," *Brain Research*, vol. 326, no. 1, pp. 47–63, 1985.

[6] M. L. Rennels, O. R. Blaumanis, and P. A. Grady, "Rapid solute transport throughout the brain via paravascular fluid pathways," *Advances in Neurology*, vol. 52, pp. 431–439, 1990.

[7] M. A. Stoodley, N. R. Jones, and C. J. Brown, "Evidence for rapid fluid flow from the subarachnoid space into the spinal cord central canal in the rat," *Brain Research*, vol. 707, pp. 155–164, 1996.

[8] L. E. Bilston, M. A. Stoodley, and D. F. Fletcher, "The influence of the relative timing of arterial and subarachnoid space pulse waves on spinal perivascular cerebrospinal fluid flow as a possible factor in syrinx development," *Journal of Neurosurgery*, vol. 112, no. 4, pp. 808–813, 2010.

[9] R. A. Lloyd, D. F. Fletcher, E. C. Clarke, and L. E. Bilston, "Chiari malformation may increase perivascular cerebrospinal fluid flow into the spinal cord: A subject-specific computational modelling study," *Journal of Biomechanics*, vol. 65, pp. 185–193, 2017.

[10] E. C. Clarke, M. A. Stoodley, and L. E. Bilston, "Changes in temporal flow characteristics of CSF in Chiari malformation Type I with and without syringomyelia: Implications for theory of syrinx development," *Journal of Neurosurgery*, vol. 118, pp. 1135–1140, 2013.

[11] E. H. Oldfield, K. Muraszko, T. H. Shawker, and N. J. Patronas, "Pathophysiology of syringomyelia associated with chiari i malformation of the cerebellar tonsils," *Journal of Neurosurgery*, vol. 80, no. 1, pp. 3–15, 1994.

[12] D. N. Levine, "The pathogenesis of syringomyelia associated with lesions at the foramen magnum: A critical review of existing theories and proposal of a new hypothesis," *Journal of the Neurological Sciences*, vol. 220, no. 1–2, pp. 3–21, 2004.

[13] B. Battal, M. Kocaoglu, N. Bulakbasi, G. Husmen, H. T. Sanal, and C. Tayfun, "Cerebrospinal fluid flow imaging by using phase-contrast MR technique," *The British Journal of Radiology*, vol. 84, no. 1004, pp. 758–765, 2011.

[14] M. F. Quigley, B. Iskandar, M. A. Quigley, M. Nicosia, and V. Haughton, "Cerebrospinal fluid flow in the foramen magnum: Temporal and spatial patterns at MR imaging in volunteers and in patients with Chiari I malformation," *Radiology*, vol. 232, no. 1, pp. 229–236, 2004.

[15] T. H. Milhorat, M. Nishikawa, R. W. Kula, and Y. D. Dlugacz, "Mechanisms of cerebellar tonsil herniation in patients with chiari malformations as guide to clinical management," *Acta Neurochirurgica*, vol. 147, no. 12, pp. 1237–1247, 2005.

[16] G. L. Nozaleda, F. J. Parras-Martos, C. Yamamoto, W. Coenen, C. Martínez-Bazán, G. Olivares-Granados, N. Cordero-Tous, V. M. Ravindra, C. Gutiérrez-Montes, and A. L. Sánchez, "Patient-specific CFD modeling of CSF flow in Chiari I malformation: denticulate-ligament-induced compartmentalization explains flow patterns," *Fluids and Barriers of the CNS*, vol. 23, no. 1, p. 54, 2026.

[17] B. L. C. Wright, J. T. F. Lai, and A. J. Sinclair, "Cerebrospinal fluid and lumbar puncture: A practical review," *Journal of Neurology*, vol. 259, pp. 1530–1545, 2012.

[18] B. A. Martin, W. Kalata, N. Shaffer, P. Fischer, M. Luciano, and F. Loth, "Hydrodynamic and longitudinal impedance analysis of cerebrospinal fluid dynamics at the craniovertebral junction in Type I Chiari malformation," *PLoS ONE*, vol. 8, no. 10, p. e75335, 2013.

[19] N. Shaffer, B. A. Martin, B. Rocque, C. Madura, O. Wieben, B. J. Iskandar, S. Dombrowski, M. Luciano, J. N. Oshinski, and F. Loth, "Cerebrospinal fluid flow impedance is elevated in Type I Chiari malformation," *Journal of Biomechanical Engineering*, vol. 136, no. 2, p. 021012, 2014.

[20] A. Ibrahimy, C.-W. C. Huang, A. F. Bezuidenhout, P. A. Allen, R. A. Bhadelia, and F. Loth, "Association between resistance to cerebrospinal fluid flow near the foramen magnum and cough-associated headache in adult Chiari malformation Type I," *Journal of Biomechanical Engineering*, vol. 143, no. 5, p. 051003, 2021.

[21] E. Öhlen, V. G. El-Hajj, V. E. Staartjes, P. Jabbour, E. Edström, and A. Elmi-Terander, "Difference in clinical presentation and surgical outcomes in pediatric and adult patients with Chiari malformation type 1: a single center retrospective study," *Acta Neurochirurgica*, vol. 167, no. 1, p. 120, 2025.

[22] A. Mortazavi, N. D. Almeida, K. Hofmann, L. Davidson, J. Rotter, T. N. Phan, D. Tsering, C. Maxwell, J. Karunakaran, E. Veznedaroglu, J. D. Heiss, F. A. Sandhu, J. S. Myseros, C. O. Oluigbo, S. N. Magge, L. D. C. Shields, M. K. Rosner, G. P. Chatain, and R. F. Keating, "Multi-center comparison of Chiari malformation type I presentation in children versus adults," *Journal of Neurosurgery: Pediatrics*, vol. 34, no. 1, pp. 49–56, 2024.

[23] B. De Leener, S. Lévy, S. M. Dupont, V. S. Fonov, N. Stikov, D. L. Collins, V. Callot, and J. Cohen-Adad, "Sct: Spinal cord toolbox, an open-source software for processing spinal cord mri data," *NeuroImage*, vol. 145, pp. 24–43, 2017.

[24] R. Kikinis, S. D. Pieper, and K. G. Vosburgh, "3d slicer: A platform for subject-specific image analysis, visualization, and clinical support," in *Intraoperative Imaging and Image-Guided Therapy*. Springer, 2013, pp. 277–289.

[25] J. Abderezaei, F. Rezayaraghi, A. Pionteck, Y.-C. Chuang, A. Carrasquilla, G. Bilgili, T. Ren, T. Lam, T. A. Lu, M. Scadeng, P. Fillingham, P. Morgenstern, M. R. Levitt, R. G. Ellenbogen, Y. Yang, S. J. Holdsworth, R. Shrivastava, and M. Kurt, "Increased hindbrain motion in chiari i malformation patients measured through 3d amplified mri (3d amri)," *Brain Multiphysics*, vol. 7, p. 100100, 2024.

[26] J. D. Heiss, G. Suffredini, K. D. Bakhtian, M. Sarntinoranont, and E. H. Oldfield, "Normalization of hindbrain morphology after decompression of chiari malformation type i," *Journal of Neurosurgery*, vol. 117, no. 5, pp. 942–946, 2012.

[27] A. Kumar, S. N. Ghosh, and S. I. Sadique, "Clinicoradiological study of adult chiari malformation type i patients with emphasis on cerebrospinal fluid peak flow velocity at foramen magnum level," *Neurology India*, vol. 67, no. 3, pp. 744–748, 2019.

[28] R. G. Ellenbogen, R. A. Armonda, D. W. W. Shaw, and H. R. Winn, "Toward a rational treatment of chiari i malformation and syringomyelia," *Neurosurgical Focus*, vol. 8, no. 3, p. E6, 2000.

[29] J. Cousins and V. Haughton, "Motion of the cerebellar tonsils in the foramen magnum during the cardiac cycle," *American Journal of Neuroradiology*, vol. 30, no. 8, pp. 1587–1588, 2009.

[30] J. R. Kröger, A. Juettner, A. Brentrup, B. Fiedler, G. Crelier, W. Schwindt, T. Niederstadt, W. Heindel, D. Maintz, and A. C. Bunck, "4d mr imaging of cerebrospinal fluid flow in chiari i malformation with and without syringomyelia and flow changes after decompressive surgery," *Journal of Cardiovascular Magnetic Resonance*, vol. 14, no. Suppl 1, p. W1, 2012.

[31] M. T. Dolar, V. M. Haughton, B. J. Iskandar, and M. Quigley, "Effect of craniocervical decompression on peak csf velocities in symptomatic patients with chiari i malformation," *American Journal of Neuroradiology*, vol. 25, no. 1, pp. 142–145, 2004.

[32] S. I. Sadique, P. Pandey, and A. K. Chaudhuri, "Cerebrospinal fluid flowmetry in pediatric patients with chiari malformation i with surgical implications," *World Neurosurgery*, vol. 135, pp. 83–86, 2020.

[33] S. Mohsenian, A. Ibrahimy, M. M. F. Al Samman, J. N. Oshinski, R. A. Bhadelia, D. L. Barrow, P. A. Allen, R. Amini, and F. Loth, "Association between resistance to cerebrospinal fluid flow and cardiac-induced brain tissue motion for chiari malformation type i," *Neuroradiology*, vol. 65, no. 10, pp. 1535–1543, 2023.

[34] M. E. Wagshul, P. K. Eide, and J. R. Madsen, "The pulsating brain: A review of experimental and clinical studies of intracranial pulsatility," *Fluids and Barriers of the CNS*, vol. 8, no. 1, p. 5, 2011.